Fibers and Polymers 2020, Vol.21, No.12, 2873-2887
DOI 10.1007/s12221-020-0026-2

ISSN 1229-9197 (print version)
ISSN 1875-0052 (electronic version)

Numerical Study of the Damage Behavior of Carbon Fiber/Glass Fiber Hybrid Composite Laminates under Low-velocity Impact

Chenxu Zhang[1,2,3], Jia Huang[4], Xi Li[5], and Chao Zhang[1,2,3]*

[1]*Department of Aeronautical Structure Engineering, Northwestern Polytechnical University, Xi'an, Shaanxi 710072, China*
[2]*Shaanxi Key Laboratory of Impact Dynamics and Its Engineering Application, Xi'an, Shaanxi 710072, China*
[3]*Joint International Research Laboratory of Impact Dynamics and Its Engineering Application, Xi'an, Shaanxi 710072, China*
[4]*School of Mechanical Engineering, University of Shanghai for Science and Technology, Shanghai 200093, China*
[5]*Structural Integrity & Composites Group, Faculty of Aerospace Engineering, Delft University of Technology,*
Kluyverweg 1, 2629HS, Netherlands

(Received January 10, 2020; Revised February 29, 2020; Accepted March 15, 2020)

Abstract: Carbon fiber-reinforced composite materials are widely employed in aircraft structures due to their high specific strength and high specific modulus. However, the poor impact resistance of carbon fiber reinforced composites creates challenges for aircraft design and maintenance. The introduction of a layer of glass fibers in the hybrid composites can effectively improve the impact performance of the composite laminate. In this work, finite element models for low-velocity impact of carbon fiber laminate and glass fiber laminate are established and validated. A VUMAT subroutine in Abaqus is implemented to evaluate the progressive damage of the composite materials, and a cohesive-zone model is employed to simulate the interface failure behavior. The impact resistance of hybrid composite laminates is systematically studied based on the results of the finite element simulation. Ten different hybrid configurations are studied and compared with a composite laminate having a single type of fiber reinforcement. The numerical results for the global mechanical response, damage modes and characteristics are extracted and systematically discussed. The results suggest that laminates having carbon fiber layers on the top and bottom surfaces with glass fiber layers between them perform the best in terms of energy absorption. When the glass fiber layers are used for the top and bottom surfaces with carbon fiber layers as the core, the presence of a carbon fiber layer with a ±45 ° orientation can help to reduce the damage area.

Keywords: Hybrid composites, Laminates, Low velocity impact, Finite element analysis (FEA), Delamination

Introduction

Compared with traditional materials, carbon fiber reinforced composites are preferable for their excellent properties, such as high specific strength, high specific modulus, low density, and design flexibility, which enable them to be widely employed in aircraft structures [1-3]. However, during its service life, an aircraft structure is vulnerable to low-velocity impacts such as those from tools dropped during maintenance, and the shock load of a low-velocity impact may cause severe but invisible damage inside the composite materials, which can significantly reduce the strength of the engineering structure and put the aircraft at risk [4-6]. In order to find a solution, some researchers have proposed hybridization to improve the impact resistance of carbon fiber reinforced composites [7-13]. Hybrid fiber reinforced composites are defined as fiber reinforced composite materials containing two or more categories of reinforcing fibers in a single matrix. A feasible approach for producing such a material is to hybridize a carbon fiber reinforced composite with glass fibers; this approach produces a composite with good ductility that is low in cost and easy to process [14-16].

In recent years, hybrid composite materials with carbon and glass fibers have been extensively studied. The initial investigations focused on the quasi-static properties [17,18] and flexural properties [19,20] of these hybrid composites. The low-velocity impact behavior of hybrid laminates has also been studied, in which the vast majority of investigations examined the impact behavior of woven hybrid composites [9,14,21-24]. Low-velocity impact studies on layer-by-layer hybridized laminates, on the other hand, are fewer in comparison. Sayer *et al.* [11] conducted an experiment to obtain the penetration and perforation limits for two types of carbon/glass hybrid laminates using an energy profiling method; their results show that the perforation threshold of a laminate with carbon layers on the impact surface is about 30 % higher than a laminate with glass layers on the impact side. Although the impact resistance of hybrid laminates is not as good as that of woven composites, additional research on low-velocity impacts to hybrid laminates is still needed, as the application of composite laminates is very extensive [25].

Early research on low-velocity impacts to hybrid composites mainly relied on impact experiments. Numerical simulation studies based on experimental data have only appeared in recent years, and only a few numerical simulation studies have been performed for low-velocity impacts of hybrid composites [12,24,26]. Barouni *et al.* [12] reported the damage characteristics of flax/glass hybrid laminates under

---

*Corresponding author: chaozhang@nwpu.edu.cn

25-J and 50-J impacts obtained from experiments and simulations using the finite element method. Only one interlaced hybrid configuration was designed for this experiment, and the damage was mainly assessed by microcomputed tomography after impact testing, with the numerical simulation results used as a supplement to the evaluation of the delamination damage observed in the experiment. Chen *et al.* [24] investigated the low-velocity impact of carbon/glass/basalt hybrid composites using experimental and numerical methods. In this study, six symmetrical sandwich-like stacking sequences were designed. The test results showed that the laminate exhibits a similar impact response when either glass or basalt fibers hybridize with carbon fibers, and the numerical simulation agrees well with the experimental results. Bandaru *et al.* [26] considered the impact performance of Kevlar/basalt fabrics, where the characterization of peak force and absorbed energy was based on experimental and numerical results; in their study, two hybrid configurations (one with an interlaced structure and one with an up-down structure) were designed, and the performance for the interlaced hybrids was found to be better than that of pure Kevlar laminate.

By reviewing the above papers, it is found that the current simulations of hybrid composites are based on experiments performed by the authors themselves, and simulation results were mainly used to supplement the experimental results. However, in the design for the laminated composites in these studies, few hybrid configurations are considered, making it difficult to analyze the damage patterns and impact resistance for different stacking sequences. Therefore, in the study described in this paper, 10 hybrid configurations were designed for the numerical simulation, including typical up-down, sandwich and staggered structures, to discover the differences in behavior. To the best of the authors' knowledge, no work has been done to investigate the influence of ±45 ° layers in hybrid laminates. Hence, the aim of this study is to gain a better understanding of low-velocity damage behavior of a hybrid composite laminate with configurations containing ±45 ° layers by using a numerical simulation.

Recently, many new numerical approaches are developed to simulate intralaminar and interlaminar damage patterns in laminated composite structures [39-43]. Zhang *et al.* [39] proposed a phase field model combined with cohesive element to simulate the progressive failure in composite. Zhi *et al.* [40] formulated a novel discontinuous solid-shell element to analyze the matrix cracking and delamination of composites. Chen *et al.* [41] presented a three-dimensional computational framework with an extended cohesive model and a global contact search algorithm to simulate the impact fracture of automotive laminated glass. Vigueras *et al.* [42] proposed an extended finite element method to simulate fracture of large-scale composite. Chen *et al.* [43] formulated a nodal-based extrinsic cohesive/contact model to discuss interfacial debonding of composite. Compared with the above-mentioned methods, the progressive damage model is more extensively utilized in low-velocity impact simulations of composite laminates [32], due to its good compatibility for implementing in commercial finite element software. Additionally, due to the excellent modeling efficiency, cohesive zone model is the most popular method to simulate the intralaminar delamination in laminate composites [44]. Therefore, in this paper, the progressive damage model and a cohesive zone model are utilized to model the intralaminar and interlaminar damage behavior of the composite laminates.

In the present study, the constitutive model and progressive damage model of the composite are first implemented in a VUMAT subroutine in Abaqus. Next, the finite element (FE) models for the two types of laminates are established and validated by comparing the FE results with the experimental results for the carbon fiber laminates and glass fiber laminates reported in the literature by Hongkarnjanakul *et al.* [27] and Singh *et al.* [28], respectively. Lastly, five groups of 10 hybrid configurations were designed and implemented in Abaqus, and their impact behavior was compared with that of regular composite laminates having a single type of fiber reinforcement (either carbon fibers or glass fibers).

Numerical Modeling

Constitutive Model

Anisotropic composite laminates can be considered as orthotropic materials because of their symmetry. Thus, the stiffness matrix of the composite laminates can be reduced to

$$C=\frac{1}{\Delta}\begin{bmatrix} E_{11}(1-\upsilon_{23}\upsilon_{32}) & E_{11}(\upsilon_{21}+\upsilon_{23}\upsilon_{31}) & E_{11}(\upsilon_{31}+\upsilon_{21}\upsilon_{32}) & & & \\ & E_{22}(1-\upsilon_{13}\upsilon_{31}) & E_{22}(\upsilon_{32}+\upsilon_{12}\upsilon_{31}) & & & \\ & & E_{33}(1-\upsilon_{12}\upsilon_{21}) & & & \\ & & & 2\Delta G_{12} & & \\ & & & & 2\Delta G_{23} & \\ & & & & & 2\Delta G_{13} \end{bmatrix} \tag{1}$$

$$\Delta = 1-\upsilon_{12}\upsilon_{21}-\upsilon_{23}\upsilon_{32}-\upsilon_{13}\upsilon_{31}-2\upsilon_{21}\upsilon_{32}\upsilon_{13} \tag{2}$$

where E is the Young's modulus; G is the shear modulus; υ is the Poisson's ratio; and the subscripts 1, 2 and 3 refer to direction along the fiber, the in-plane direction perpendicular to the fiber, and the out-of-plane direction perpendicular to the fiber, respectively.

Intralaminar Damage Model

Damage Initiation

Intralaminar damage modes of composite laminates include fiber breakage, matrix cracking, and matrix crushing. For the low-velocity impact simulations conducted in this study, fiber damage generally does not occur under such a small impact energy [27,28]. Therefore, the maximum stress criterion is selected as the fiber failure criterion for the damage model.

The fiber tensile failure criterion is defined as

$$r_{ft} = \left(\frac{\sigma_{11}}{X_T}\right)^2 (\sigma_{11} > 0) \tag{3}$$

where r_{ft} is the failure indicator for judging the fiber tensile damage and where X_T is the tensile strength in the direction of the fibers.

The fiber compression failure criterion is defined as

$$r_{fc} = \left(\frac{\sigma_{11}}{X_C}\right)^2 (\sigma_{11} < 0) \tag{4}$$

where r_{fc} is the failure indicator for judging the fiber compression damage and where X_C is the compressive strength in the direction of the fiber.

The matrix cracking and matrix crushing failure criteria used in this study are defined by the Hou [29,30] damage model. The matrix tensile failure criterion is defined as

$$r_{mt} = \left(\frac{\sigma_{22}}{Y_T}\right)^2 + \left(\frac{\sigma_{12}}{S_{12}}\right)^2 + \left(\frac{\sigma_{23}}{S_{23}}\right)^2 (\sigma_{22} > 0) \tag{5}$$

where r_{mt} is the failure indicator for judging the matrix tensile damage, Y_T is the tensile strength in the transverse direction, and S_{12} and S_{23} are shear strengths.

The matrix compression failure criterion is defined as

$$r_{mc} = \frac{1}{4}\left(\frac{-\sigma_{22}}{S_{12}}\right)^2 + \frac{Y_C^2\sigma_{22}}{4S_{12}^2 Y_C} - \frac{\sigma_{22}}{Y_C} + \left(\frac{\sigma_{12}}{S_{12}}\right)^2 (\sigma_{22} < 0) \tag{6}$$

where r_{mc} is the failure indicator for judging the matrix compression damage and where Y_C is the compressive strength in the transverse direction.

Damage Evolution

Damage evolution describes the process where the stiffness of the laminate degrades after damage is initiated. At present, the commonly used damage evolution schemes reduce the stiffness in the direction of damage growth according to different damage modes, thereby reducing the load carrying capacity of the composite material. The equivalent-strain method based on the critical fracture energy of the element is used in this study is based on that of Tan *et al.* [31] and Li *et al.* [32], in which the damage variable is defined as

$$d_i = \frac{\varepsilon_{eq,i}^f(\varepsilon_{eq,i} - \varepsilon_{eq,i}^0)}{\varepsilon_{eq,i}(\varepsilon_{eq,i}^f - \varepsilon_{eq,i}^0)} \tag{7}$$

where i represents the four different modes of damage (tensile and compressive damage of the fiber and matrix) and where $\varepsilon_{eq,i}$, $\varepsilon_{eq,i}^0$ and $\varepsilon_{eq,i}^f$ are the equivalent strain, damage initiation strain and final failure strain, respectively. The damage initiation strain is obtained by $\varepsilon_{eq,i}^0 = X_i/E_{0,j}$, and the final failure strain is obtained by $\varepsilon_{eq,i}^f = 2G_i/X_i l_c$, where X_i is the strength value of the material, $E_{0,j}$ is the initial modulus value, G_i is the critical fracture energy of the material, and l_c is the characteristic length. The characteristic length is introduced in order to eliminate the grid correlation in the finite element model, which is in the direction along the crack propagation. The parameter $\varepsilon_{eq,i}$ usually refers to the strain along the fiber direction (for fiber damage) and the strain in the transverse direction (for matrix damage).

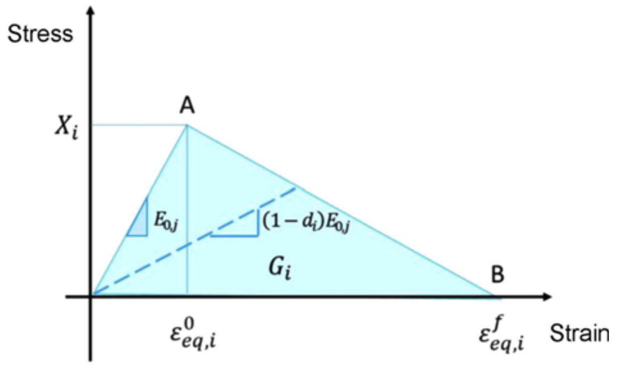

Figure 1. Relationship between equivalent stress and equivalent strain.

The relationship between equivalent stress and equivalent strain is shown in Figure 1. From this figure, it can be noticed that the fracture energy G_i is the area of the triangle, Point A is the location of damage initiation, and Point B is the final failure position.

Damage Constitutive Model

After damage is initiated, the damage stiffness matrix is considered in the constitutive model, which is defined as

$$C_d = \frac{1}{\Delta}\begin{bmatrix} d_f E_{11}(1-d_m\upsilon_{23}\upsilon_{32}) & d_f d_m E_{11}(\upsilon_{21}+\upsilon_{23}\upsilon_{31}) & d_f E_{11}(\upsilon_{31}+\upsilon_{21}\upsilon_{32}) & & & \\ & d_m E_{22}(1-d_f\upsilon_{13}\upsilon_{31}) & d_m E_{22}(\upsilon_{32}+d_f\upsilon_{12}\upsilon_{31}) & & & \\ & & E_{33}(1-d_f d_m\upsilon_{12}\upsilon_{21}) & & & \\ & & & 2\Delta d_f d_m G_{12} & & \\ & & & & 2\Delta d_f d_m G_{23} & \\ & & & & & 2\Delta d_f d_m G_{13} \end{bmatrix} \tag{8}$$

$$\Delta = 1 - d_f d_m \upsilon_{12}\upsilon_{21} - d_m\upsilon_{23}\upsilon_{32} - d_f\upsilon_{13}\upsilon_{31} - 2d_f d_m\upsilon_{21}\upsilon_{32}\upsilon_{13} \tag{9}$$

where d_f and d_m are coupled damage variables, which are given as

$$d_f = (1-d_{ft})(1-d_{fc}) \tag{10}$$

$$d_m = \max((1-S_{mt}d_{mt})^2, (1-S_{mc}d_{mc})^2) \tag{11}$$

where S_{mt} and S_{mc} are the stiffness degradation control factors caused by matrix tensile and compressive damage, respectively. In the constitutive model for this study, the values for S_{mt}=0.9 and S_{mc}=0.5 were adopted from Lee *et al.* [33] and Liao and Liu [34], respectively. The same values of these two factors are also used in other literatures for simulating low-velocity impact damage of composite laminates [45-47].

Interlaminar Damage Model

To simulate interlaminar damage of the composite materials, a cohesive method based on damage mechanics and the bilinear traction-separation law was utilized in this study. Similar to an intralaminar damage model, an interlaminar damage model includes a damage initiation criterion and an evolution criterion. The damage initiation criterion adopts the quadratic nominal stress failure criterion from Sokolinsky *et al*. [35], which is shown in equation (12):

$$\left\{\frac{\langle t_n\rangle}{t_n^0}\right\}^2+\left\{\frac{t_s}{t_s^0}\right\}^2+\left\{\frac{t_t}{t_t^0}\right\}^2=1 \tag{12}$$

where t_n^0, t_s^0, and t_t^0 are strengths in the normal and shear directions and where t_n, t_s, and t_t are tractions in the normal and shear directions. In this expression, a Macaulay bracket was used to exclude compressive stress states.

The damage evolution criterion adopts the B-K criterion of Benzeggah and Kenane [36] based on the fracture mechanics:

$$G_n^C+(G_s^C-G_n^C)\left\{\frac{G_S}{G_T}\right\}^{\eta}=G^C \tag{13}$$

where $G_S = G_s + G_t$, $G_T = G_n + G_s + G_t$. In this equation, G_n G_s, and G_t are the dissipated energy in the normal and shear directions; G_n^C, G_s^C, and G_t^C are the corresponding critical dissipated energies; and η is a material constant that is set to 1.45, after Liao and Liu [34].

Finite Element Model for the Carbon Fiber Laminate

The finite element model for the carbon fiber laminate in this study was established in Abaqus and was based on the experimental setup in Hongkarnjanakul *et al*. [27], where an impact experiment was carried out for a T700/M21 carbon fiber laminate panel using a drop-testing machine with a 16-mm-diameter impactor and a 2-kg weight, according to test standard AITM 1-0010 (Compression After Impact). The velocity of the impactor prior to impact was measured by an optical laser velocimeter, and the contact force between the impactor and the laminate was recorded by a piezoelectric power sensor inside the impactor. To verify the accuracy of the FE model, the results for the FE model were compared with the experimental data of Hongkarnjanakul *et al*. [27].

As shown in Figure 2, the FE model consists of three parts: a composite laminate, a rigid impactor, and a rigid frame. The size of the laminate used in the test by Hongkarnjanakul *et al*. was 150 mm×100 mm×4 mm, and the stacking sequence was $[0_2, 45_2, 90_2, -45_2]_s$. The material parameters for the T700/M21 carbon fiber laminate are shown in Table 1.

In order to simplify the model and improve the calculation efficiency, the two adjacent layers with the same material direction are regarded as a single layer. As a result, the final model has a total of eight layers, and the thickness of each layer is 0.5 mm. Each layer of the laminate adopts a three-dimensional eight-node reduction integral element (C3D8R). A zero-thickness cohesive interface is inserted between every two layers, using a three-dimensional eight-node cohesive element (COH3D8). The mesh of the center area (72 mm×

Table 1. Material parameters for a T700/M21 carbon fiber laminate

Intralaminar parameters	Density	ρ=1600 kg/m^3
	Young's modulus	E_{11}=130 GPa, E_{22}=E_{33}=7.7 GPa G_{23}=3.8 GPa, G_{12}=G_{13}=4.8 GPa
	Poisson's ratio	υ_{23}=0.35, υ_{12}=υ_{13}=0.33
	Strength	X_T=2080 MPa, X_C=1250 MPa Y_T=Z_T=60 MPa, Y_C=Z_C=140 MPa S_{12}=S_{13}=S_{23}=110 MPa
	Fracture energy	G_{ft}=133 N/mm, G_{fc}=40 N/mm G_{mt}=0.6 N/mm, G_{mc}=2.1 N/mm
Interlaminar parameters	Strength	T_1^0=T_2^0=T_3^0=30 MPa
	Stiffness	5000 N/mm^3
	Fracture energy	G_1^c=0.6 N/mm, G_2^c=G_3^c=2.1 N/mm

Note: The parameters listed in this table were obtained from Hongkarnjanakul *et al*. [27] and Liao and Liu [34].

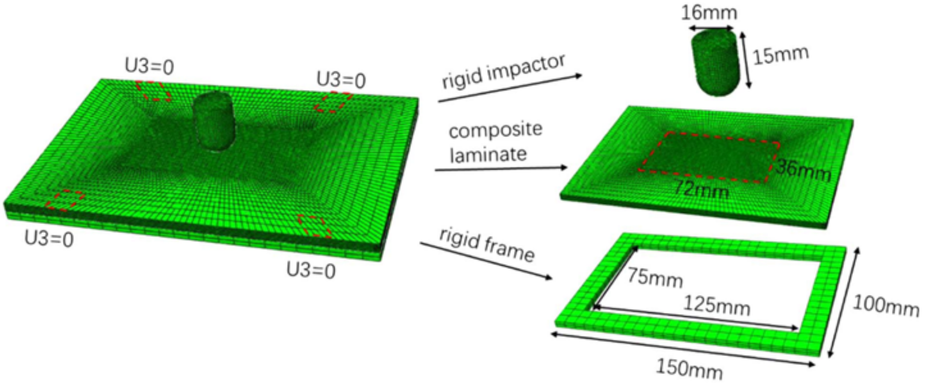

Figure 2. Finite element model for low-velocity impact of carbon fiber composites.

36 mm) of the laminate is refined to the element size of 1.2 mm×0.9 mm×0.5 mm. The mesh size becomes larger with the increase in distance from the laminate center. The total number of laminate elements in the final model is 82,889.

For the impactor, which is regarded as a discrete rigid body, a three-dimensional four-node bilinear rigid quadrilateral element (R3D4) is adopted. A reference point is utilized to define a rigid body constraint for the impactor such that all properties of the impactor can be assigned to the reference point. According to the experimental setup, the front of the impactor has a hemispherical shape with a diameter of 16 mm. The mass of the impactor is 2 kg and the impact velocity is 5 m/s, which is equivalent to an impact energy of 25 J. A rigid frame with an inner area of 125 mm×75 mm is also assigned to the rigid body constraint as a support for the laminate. All degrees of freedom of the rigid frame are constrained, and the nodes at the four corners of the laminate (the four red parallelograms of Figure 2) are selected to restrain the Z-axis displacement. Hence, the out-of-plane displacement of the laminate in the Z direction is constrained as well. For the impactor, only the degree of freedom along the Z direction is not constrained; this ensures that the FE model will be consistent with the experiment.

Since penetration does not occur during a low-velocity impact [27,28], a general contact can be applied to the entire model. Hard contact is adopted as the interaction property for normal contact behavior, and the penalty function method with a friction coefficient setting of 0.3 is employed for the tangential contact behavior. Finally, the total impact time of the simulation is set to 4 ms.

Finite Element Model for the Glass Fiber Laminate

An experiment described in a paper published in 2015 by Singh *et al.* [28] was used to establish the finite element model for the glass fiber in this study. Similar to the experiment in Hongkarnjanakul *et al.*, the impact test was conducted by a drop-weight device, but the dimensions of the specimen used by Singh *et al.* was 175 mm×175 mm×6.4 mm. Digital image correlation (DIC) was used to record the deformation and strains of the specimen. The experimental data from Singh *et al.* were compared with the simulation results in order to verify the FE model.

The FE model for glass fiber consists of only two parts: the impactor and the composite laminate (as shown in Figure 3). The size of the laminate is 125 mm×125 mm×6.4 mm with a total of eight 0.8-mm-thick layers, which is the same number of layers and the same layer thickness as the model for glass fiber reported in Singh *et al.* [28], and the same stacking sequence for the laminate ($[0]_8$) is used as well. The material parameters of a common type of glass fiber (E-glass, which is composed of alumino-borosilicate glass with less than 1 % w/w alkali oxides) that was used in the FE model simulation in this study are listed in Table 2, and these parameters were further calibrated against those for the experimental results.

In order to simulate the delamination behavior, a cohesive layer is inserted between each layer, even though the fiber orientation of each layer is uniform. The element used for the cohesive interface is still an eight-node three-dimensional cohesive element (COH3D8), while the composite plies of the laminate use a three-dimensional eight-node completely integral element (C3D8) to keep consistent with the choice in Ref. [28]. The mesh size of the 50 mm×50 mm refined area around the impact point is 1 mm×1 mm×0.8 mm, and the total number of elements is 48000. The element type of the impactor is the same as that for the impactor used in the

Table 2. Material parameters for E-glass composite

Intralaminar parameters	Density	ρ=1780 kg/m^3
	Young's modulus	E_{11}=40 GPa, E_{22}=E_{33}=10 GPa G_{23}=4.32 GPa, G_{12}=G_{13}=3.15 GPa
	Poisson's ratio	υ_{23}=0.21, υ_{12}=υ_{13}=0.3
	Strength	X_T=988 MPa, X_C=1432 MPa Y_T=Z_T=44 MPa, Y_C=Z_C=285 MPa S_{12}=S_{13}=60.6, S_{23}=22 MPa
	Fracture energy*	G_{ft}=80 N/mm, G_{fc}=25 N/mm G_{mt}=0.15 N/mm, G_{mc}=1 N/mm
Interlaminar parameters	Strength*	T_1^0=T_2^0=T_3^0=29 MPa
	Stiffness*	10000 N/mm^3
	Fracture energy*	G_1^c=0.5 N/mm, G_2^c=G_3^c=1.55 N/mm

*Parameters reported by Lapczyk and Hurtado [38]. All other parameters were reported by Singh *et al.* [28].

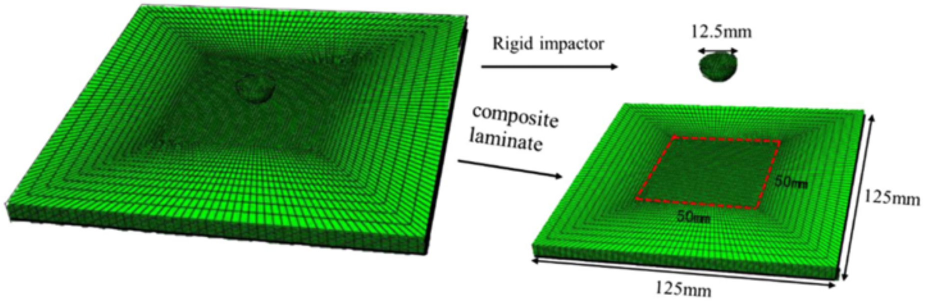

Figure 3. Finite element model for low-velocity impact of glass fiber composites.

FE model for the carbon laminate, and the impactor has a hemispheric shape with a diameter of 12.5 mm. The impactor used in the FE model for the glass laminate, however, has a mass of 1.475 kg and an impact velocity of 4 m/s, which corresponds to an impact energy of 12.7 J. The major difference between the glass fiber model and the carbon fiber model is the boundary condition of the laminate in the glass fiber model: since there is no rigid frame used as a support, the six degrees of freedom for the four sides of the laminate are constrained to keep the model consistent with the experimental results reported by Singh *et al*. [28]. For the definition of contact, the coefficient of friction in the glass model is set to 0.2, and the remaining settings are the same as those previously described for the carbon fiber model. The total time of the impact is set to 3.5 ms.

Results and Discussion

Validation of Model for Carbon Fiber Laminate

The numerical simulation results are compared with the experimental results to validate the accuracy of the model, i.e., the force-time curve, the force-displacement curve, and the overlapping delamination damage area measured by the C-scan, as shown in Figure 4. As can be noticed from Figure 4(a), both curves show a slight decreasing tendency at the beginning of the impact. The two curves show a similar increase until they reach the peak force before declining during the rebounding stage. The peak contact force and the time at the instant of reaching peak force, as well as the total impact period predicted by the numerical model, all match well with the measurements obtained in the experiments. In Figure 4(b), the displacement obtained from the simulation increases with the contact force and reaches the peak value at the same time point as in the experiment, and it rebounds to zero after reaching the peak value, which is also consistent with the experimental results. Although the peak displacement value in the FE model is slightly larger than that reported in the experiment, the curvatures of the numerical and experimental curves agree very well, especially for the rebound phase in the force-displacement diagram. Figure 4(c) shows a comparison of the numerical prediction for the delamination area to the area measured in the experiment; the two are in good agreement, except that the sizes of the predicted delamination areas for the top few interface layers near the impact side are slightly larger than those reported in the experimental results. Overall, the numerical simulation realized by using the VUMAT subroutine in Abaqus is well validated; thus, it can be used to accurately predict the low-velocity impact behavior of a carbon fiber composite laminate.

Validation of Model for Glass Fiber Laminate

The comparison between the low-velocity simulation and the experimental results for the glass fiber laminate is shown in Figure 5, through an impact force-time curve, a displacement-time curve and a strain-time curve of the node 15 mm from the impact center along the fiber direction, as well as from contour maps of the projected damage.

As can be seen from Figure 5(a), the peak of the contact force in the numerical prediction is larger and the contact time of the simulation is longer than those observed in the experiment, while the maximum displacement for the numerical prediction is smaller, as shown in Figure 5(b).

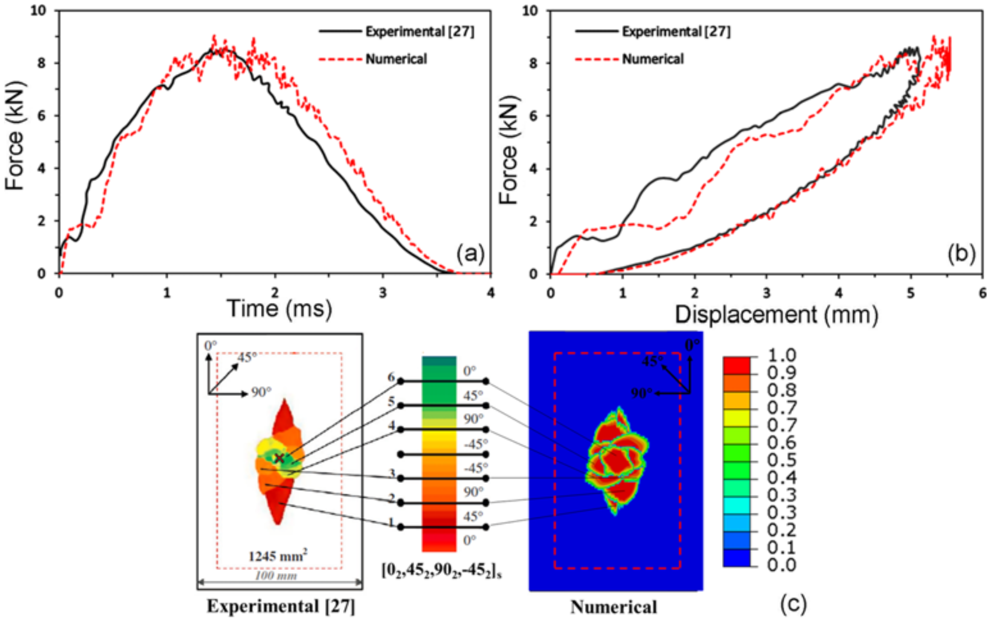

Figure 4. Comparison of the simulation results with experimental results for the carbon fiber laminate [27]; (a) force-time curves, (b) force-displacement curves, and (c) comparison of delamination areas.

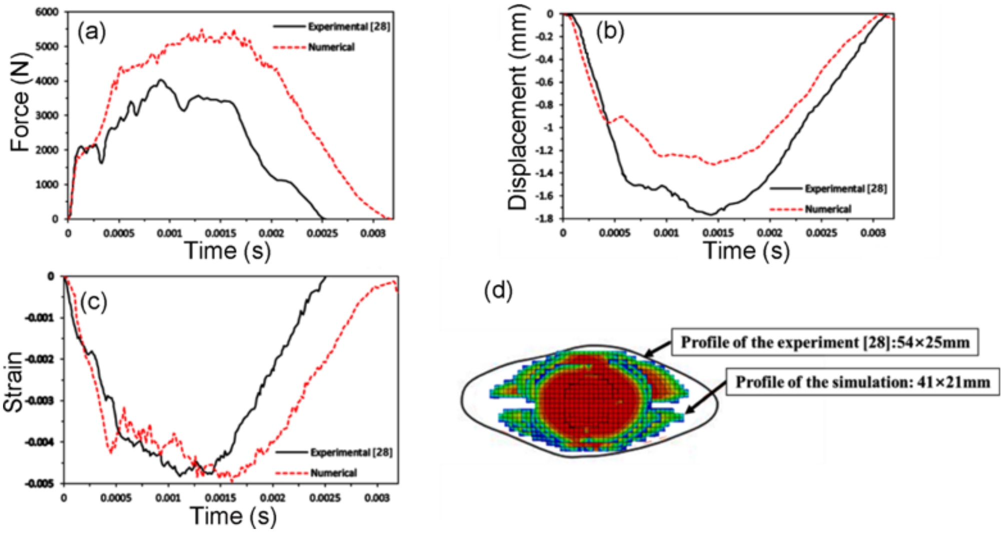

Figure 5. Comparison of the simulation results with experimental results for the glass fiber laminate [28]: (a) force-time curves, (b) displacement-time curves, (c) strain-time curves, and (d) overlapping delamination areas.

From Figure 5(c), the predictions for the initial curvature and the peak strain value for the strain-time curve are compared with those of the experimental results. The reason for the mismatch in the latter stage of the curves in Figures 5(a), (b) and (c) can be explained by the presence of permanent deformation in the impacted laminate, as observed in the experiment. This permanent deformation indicates that the epoxy matrix has undergone plastic deformation; however, the current FE model assumes that the laminate is linearly elastic, and it does not take into consideration the nonlinear plasticity. Hence, the accuracy of the model can be further improved through the incorporation of the plastic damage failure evolution, which will be investigated in a future work. For the sake of simplicity, in the current work, the plasticity effect is not considered in the model. And the focus of this work is investigating the impact resistance and energy absorption efficiency of the hybrid composite laminates.

Low-Velocity Impact Behavior of Hybrid Composite Laminate

The FE model for the carbon/glass hybrid composite laminate is established based on the model of the carbon fiber laminate described in previous section (Finite Element Models) and is achieved by adjusting the stacking sequences for each configuration and the material properties for each layer. Through an investigation of relevant studies in the literature [9,11,23,24], a total of 12 configurations were designed, as listed in Table 3. The mechanical properties of the carbon fiber plies, the glass fiber plies, and their cohesive plies are set according to the parameters listed in Tables 1 and 2. It should be noted that, for purposes of simplification, the properties of the cohesive ply between the carbon ply and the glass ply are assumed to be the average of the properties for pure carbon cohesive plies and pure glass cohesive plies (Table 4). Case 1 and Case 2 (in Table 3) correspond to pure glass fiber laminates and pure carbon fiber laminates, respectively, which have been included for comparison purposes.

Table 3. Configurations for the carbon/glass hybrid composite laminates investigated in this study

Case number	Name	Configuration
1	GGGG	$[0/90/0/90/90/0/90/0]_G$
2	CCCC	$[0/90/0/90/90/0/90/0]_C$
3	CCGG	$[0/90/0/90]_C[90/0/90/0]_G$
4	GGCC	$[0/90/0/90]_G[90/0/90/0]_C$
5	GCCG	$[0/90]_G[0/90/90/0]_C[90/0]_G$
6	CGGC	$[0/90]_C[0/90/90/0]_G[90/0]_C$
7	GCGC	$[0/90]_G[0/90]_C[90/0]_G[90/0]_C$
8	CGCG	$[0/90]_C[0/90]_G[90/0]_C[90/0]_G$
9	CCCG	$[0/90/45/-45/90/0]_C[90/0]_G$
10	GGGC	$[0/90/45/-45/90/0]_G[90/0]_C$
11	GCCG±45	$[0/90]_G[0/45/-45/0]_C[90/0]_G$
12	CGGC±45	$[0/90]_C[0/45/-45/0]_G[90/0]_C$

Table 4. Properties of the cohesive plies between the carbon plies and glass plies

Interlaminar parameters	Strength	$T_1^0=T_2^0=T_3^0=29.5$ MPa
	Stiffness	7500 N/mm^3
	Fracture energy	$G_1^c=0.55$ N/mm, $G_2^c=G_3^c=1.83$ N/mm

Global Mechanical Response

The curves of the contact force versus the impactor displacement are presented in Figure 6. In Figure 6(a), the curves for the six hybrid laminates (Cases 3 to 8) that contain only 0 ° and 90 ° layers are compared to those of the two reinforced laminates with a single type of fiber configurations (CCCC and GGGG), while the curves for the four hybrid configurations incorporating the ±45 ° plies (Cases 9 to 12) are included in Figure 6(b), along with the curves for configurations CCCC and GGGG. To investigate the influence of ±45 ° plies on the low-velocity impact resistance of composite laminates, the curves of two additional configurations (CGGC and GCCG, which have the same stacking sequence as CGGC±45 and GCCG±45, respectively, but contain only 0 ° and 90 ° layers) are also included in Figure 6(b) to allow a comparison to be made. As can be noticed from Figures 6(a) and 6(b), all curves show the same trend: the contact force increases with the increase in the displacement, gradually decreases after reaching the peak, and forms a closed loop. The oscillation of the curve is due to the onset and evolution of matrix and delamination damage. As discussed in other studies in the literature [10,25], the first drop in contact force is caused by matrix cracking or the delamination of the laminate.

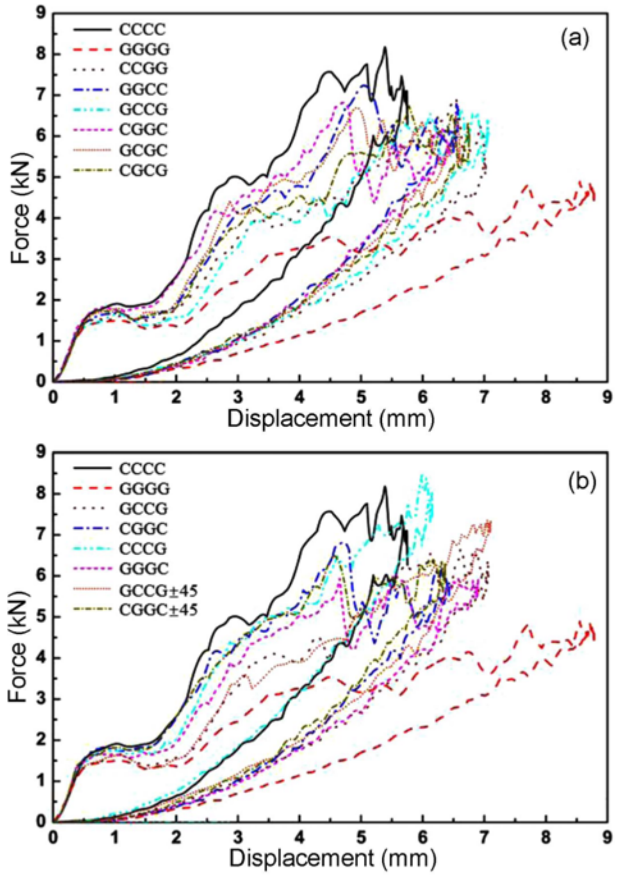

Figure 6. Force-displacement curves for composite laminates under low-velocity impact; (a) hybrid configurations without ±45 ° plies (with configurations CCCC and GGGG included for comparison purposes) and (b) hybrid configurations with ±45 ° plies (with configurations CCCC, GGGG, GCCG and CGGC included for comparison purposes).

From the curves shown in Figure 6(a), it can be clearly seen that the macroscopic mechanical responses of laminates are closely related to the positions of the carbon and glass fiber layers, and the performance of the hybrid laminates is between that of the two reinforced laminates having a single type of fiber (CCCC and GGGG). As compared to GGCC, the performance of CCGG is closer to that of GGGG, indicating that the back half of the laminate has a greater influence on the low-velocity impact response than the front half which is consistent with the findings of Khan [22]. When carbon fiber layers and glass fiber layers are mixed in a more staggered configuration, the responses of laminates are more similar. In other words, the responses of GCGC and CGCG show more similarity as compared to the responses of CCGG and GGCC.

The performance of the laminates changes significantly with the addition of ±45 ° layers. As can be seen from Figure 6(b), since there are six layers of carbon fiber in the CCCG configuration, its performance is closer to that of CCCC. In contrast, the performance of the GGGC configuration is closer to that of GGGG. The differences in the global mechanical responses of CGGC and CGGC±45 are very small, while curves of GCCG and GCCG±45 are quite distinct. This indicates that the ±45 ° layers have a greater influence on the response of the carbon fiber layers and less of an effect on the glass fiber layers.

For analyzing the impact resistance of the laminates, four indicators from the above graph have been summarized in Table 5 to enable a comparative analysis for the various hybrid laminates. To provide a better visualization that allows for easier comparison, a histogram for each parameter has been included in Figure 7. The four parameters are the peak force, the maximum displacement, the absorbed energy (which is obtained by calculating the area enclosed in the force-displacement curve) and the damping index [10]. The damping index is defined as:

$$DI = \frac{E_a}{E_e} \tag{14}$$

where E_a is the absorbed energy and E_e is the elastic energy, which is the difference of the maximum energy absorbed by the laminate and the final absorbed energy during the impact process [10]. A configuration with a lower damping index will demonstrate better impact resistance, with a larger amount of energy transferred back to the impactor [10].

The peak forces for all configurations, which represent the carrying capacity of the laminates [37], are shown in Figure 7(a). Except for CCCG, the peak force for CCCC is the largest, while that for GGGG is the smallest, which is

Table 5. Comparison of numerical parameters reflecting impact events for different hybrid configurations

	Peak force (N)	Maximum displacement (mm)	Total absorbed energy (J)	Damping index
GGGG	4920.21	8.78	11.05	0.76
CCCC	8369.54	5.75	12.99	1.04
CCGG	6924.07	7.02	13.62	1.16
GGCC	7246.20	6.57	13.33	1.06
GCCG	6985.54	7.07	12.31	0.92
CGGC	6985.09	6.43	14.03	1.24
GCGC	6745.60	6.60	13.85	1.16
CGCG	6743.40	6.76	12.84	1.03
CCCG	8449.19	6.16	9.99	0.64
GGGC	6170.64	6.90	13.05	1.05
GCCG±45	7655.01	7.10	10.47	0.68
CGGC±45	6632.35	6.37	13.42	1.13

attributed to the high strength of carbon fiber and the low strength of glass fiber. In the hybrid laminates without ±45 ° plies, GGCC has the largest peak force: 7246.20 N, which is 4.65 % higher than that of CCGG (6924.07 N). However, the position of the carbon and glass fiber layers in the "sandwich" configurations (GCCG and CGGC) and the "staggered" configurations (GCGC and CGCG) have little influence on the peak force. After adding ±45 ° layers to the carbon fiber layers (configuration GCCG±45), the peak force increased by 9.58 % comparing with that of GCCG, while the peak force of CGGC±45 decreased by 5.05 % comparing with that of CGGC. This indicates that the ±45 ° layers placed in the carbon fiber layer help to increase the peak force of the laminate. In this case, the peak force for CCCG is 0.95 % higher than that of CCCC, even though it contains a glass fiber layer.

From Figure 7(b), it can be observed that the maximum displacement of GGGG is the highest, while that for CCCC is minimal. The maximum displacements for all the hybrid composites are between those for the configurations having a single fiber type (CCCC and GGGG). Except for CCCG and GGGC, the hybrid structures with glass fiber layers on the back side (CCGG, GCCG and CGCG) have larger maximum displacements than those of the configurations with carbon fiber layers on the back side (GGCC, CGGC and GCGC). This indicates that the glass fiber layers can help enhance the impact toughness when placed at the back side of the laminate, resulting in a larger maximum displacement. In addition, it can be noticed that the introduction of ±45 ° layers of carbon fiber has only a negligible effect on the maximum displacement.

The energy absorption histogram of the single-fiber laminates and the hybrid structures is presented in Figure 7(c). It can be seen that for the laminates having a single type of fiber, CCCC absorbs more energy than GGGG. In

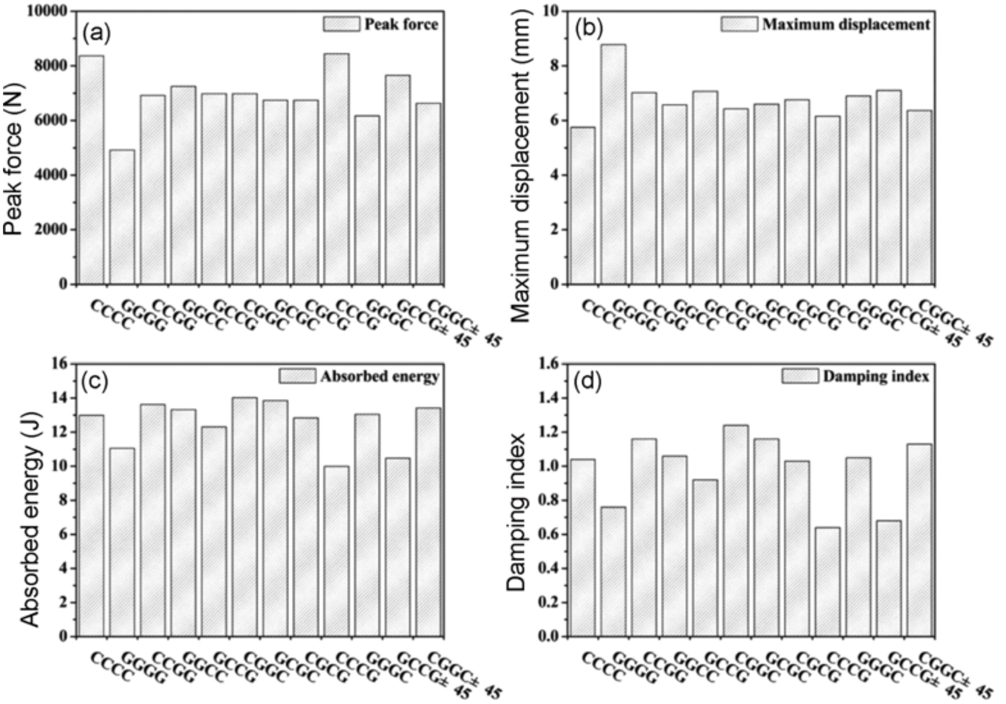

Figure 7. Comparison of characteristics of impact events for different configurations; (a) peak force, (b) maximum displacement, (c) absorbed energy, and (d) damping index.

addition, most of the hybrid configurations (CCGG, GGCC, CGGC, GCGC, GGGC and CGGC±45) absorb more energy than CCCC, in which CGGC absorbs the most energy (3.01 % more than CCCC). Due to the introduction of ±45 ° layers, configuration GCCG±45 absorbs 14.87 % less energy than GCCG, while CGGC±45 absorbs 4.35 % less energy than CGGC. This further demonstrates that the effects of the ±45 ° layers on the energy absorption are more pronounced in carbon fiber layers than in glass fiber layers. When ±45 ° layers are incorporated into the carbon fiber layers of CCCG and GCCG±45, they absorb less energy than GGGG, and configuration CCCG absorbs a minimal amount of energy. The trend observed in the histogram for the damping index in Figure 7(d) is similar to that in the histogram for energy absorption in Figure 7(c), with CGGC having the highest damping index and CCCG having the lowest. This suggests that configuration CCCG has the best impact resistance of all the studied hybrid laminates.

Low-velocity Impact Damage Behavior of Hybrid Laminates

To further understand the impact resistance and failure mechanism of hybrid composite laminates, the damage contours for laminates of different configurations were systematically studied and compared. In a low-velocity impact scenario, the main damage modes for composite laminates include matrix tensile damage, matrix compression damage and delamination damage. These damage modes are discussed in more detail in the following subsections.

Matrix Tensile Damage

The matrix tensile damage in each layer of the hybrid laminates is shown in the damage contours presented in Figure 8. In general, the damage distribution is along the fiber direction of each layer. It can be seen from the comparison group of laminates with a single type of fiber reinforcement that the area of matrix tensile damage is generally greater in the intermediate layers that are toward the back of the impact side, while the damage area in the first two layers of configuration CCCC is greater than that in the third and fourth layers. This phenomenon can be explained by the complementary effects of matrix tensile and compressive damage in the corresponding two layers [1]. It is found that the area of tensile damage in each layer of GGGG is much larger than that in each layer of CCCC, indicating that glass fiber layers are more susceptible to matrix tensile damage. However, the absorbed energy of GGGG due to matrix tensile damage is no larger than that for CCCC during the impact process.

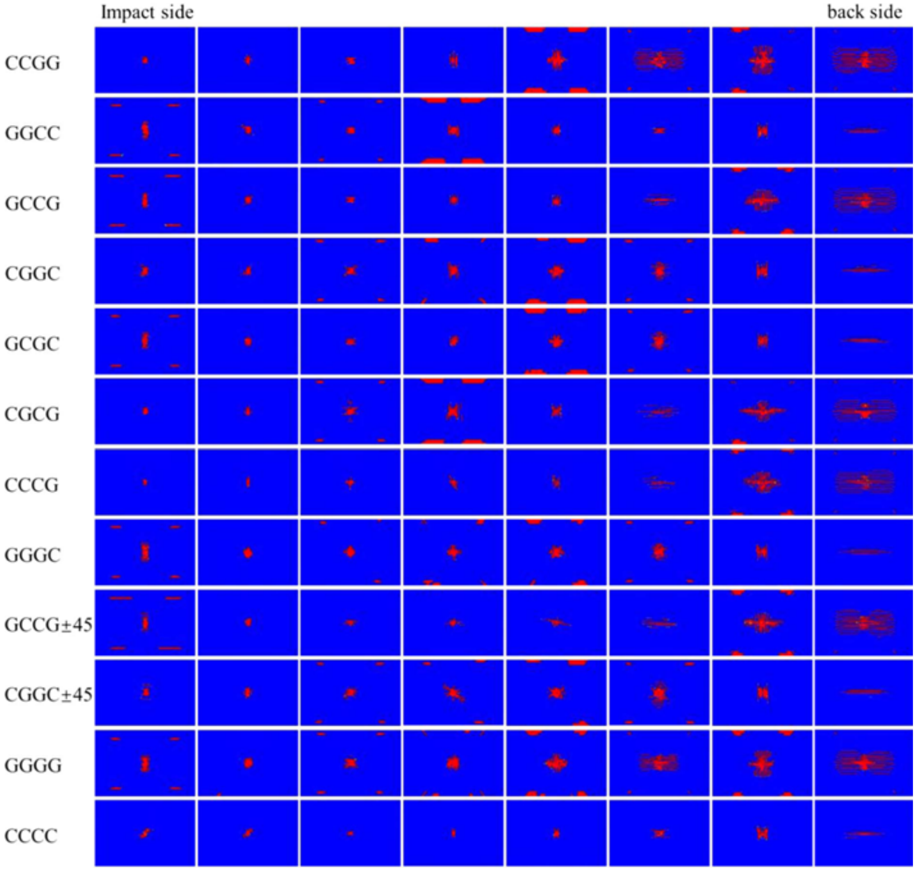

Figure 8. Comparison of matrix tensile damage contours in each ply of hybrid composites under a low-velocity impact of 25 J.

Considering the matrix tensile damage in hybrid configurations without ±45 ° plies, the area of damage in the third and fourth carbon layers in configurations CCGG, GCCG and GCGC is larger than that of the corresponding layers in CCCC, while the third and fourth glass layers in GGCC, CGGC, and CGCG show the reverse trend. For configuration CCCG, the area of damage for the carbon fiber layers closest to the impact side is smaller than that observed for CCCC, while the areas of damage in the other carbon fiber layers is larger. In contrast, the area of damage in the glass fiber layers in configuration GGGC is smaller than that of GGGG.

With the introduction of the ±45 ° layers to the laminate, the damage area for each ply of configuration GCCG±45 changes slightly as compared to the corresponding laminate without ±45 ° layers (GCCG), and the damage of the middle four layers of CGGC±45 are larger than those in the corresponding laminate without ±45 ° layers (CGGC). This suggests that the incorporation of ±45 ° layers leads to greater matrix tensile damage in the glass fiber layers. In general, since a glass fiber layer has lower tensile strength, the matrix tensile damage of the glass fiber layers that are near the back side of the laminate makes these layers relatively susceptible to failure. Therefore, the matrix tensile damage in configurations GGCC, CGGC, GCGC, GGGC, and CGGC±45 are generally small. Of these, GGCC has the area of smallest damage, while the damage areas of the other four configurations are similar but slightly higher.

Matrix Compression Damage

As can be noticed from Figure 9, the areas of matrix compression damage for all configurations are relatively small as compared to the areas of matrix tensile damage (Figure 8). Matrix compression damage presents mainly in the first two layers on the impact side. The areas of matrix compression damage for GGGG are also larger than that of the corresponding layers in CCCC, indicating that a glass fiber layer is more susceptible to matrix damage than a carbon fiber layer. Virtually no matrix compression damage was observed in the middle four layers of CCCC. For hybrid configurations without ±45 ° layers that have carbon fiber layers in the middle (CCGG, GGCC, GCCG, GCGC and CGCG), matrix compression damage can be seen in the middle carbon fiber layers of the laminates. This indicates that with the introduction of glass fiber layers, compression damage in the middle layers of the hybrid laminate may become larger.

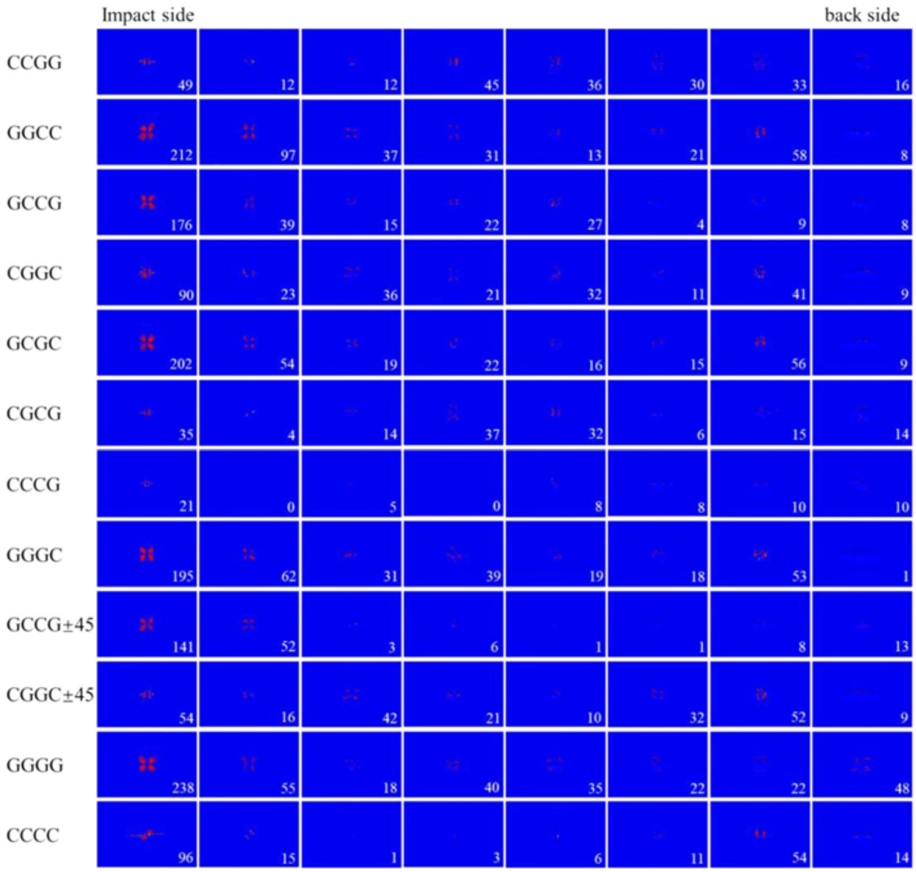

Figure 9. Comparison of matrix compression damage contours in each ply of hybrid composites under a low-velocity impact of 25 J (marked numbers represent the area of matrix compression damage because some contours are invisible and the unit is mm^2).

The compression damage in the glass fiber layers for hybrid configurations without ±45 ° layers (CCGG, GGCC, GCCG, CGGC, GCGC and CGCG) are similar to that in GGGG, which suggests that the presence of carbon fiber layers has little influence on the matrix compression damage. By comparing GCCG with the corresponding configuration with ±45 ° layers (GCCG±45), it can be noticed that the matrix compression damage is smaller with the introduction of ±45 ° layers. Little damage is apparent in the ±45 ° carbon fiber layers of the CCCG and GCCG±45 configurations, which demonstrates that ±45 ° layers can help reduce the matrix compression damage of the carbon layers. In contrast, ±45 ° layers in glass fiber layers do not provide any improvement in resistance to matrix compression damage. Since glass fiber layers are more likely to be damaged by matrix compression, compression damage to the carbon fiber layers near the impact side is somewhat smaller. In terms of both matrix tensile damage and matrix compression damage, the areas of damage in configurations with glass layers sandwiched between two carbon layers (CGGC and CGGC±45) are the smallest of all the configurations.

Delamination Damage

Figure 10 shows the interlaminar delamination damage in each interlaminar layer for all configurations. Overall, the area of delamination damage is obviously larger than that for matrix-type damage, suggesting that delamination is the main damage mode for a low-velocity impact load. From Figure 10, it can be noticed that the delamination damage in the interfaces near the top and bottom surfaces in configuration CCCC is larger than that for the intermediate interfaces, while the delamination area of GGGG shows the opposite trend. Moreover, while the interfacial damage in the top and bottom interfaces in pure glass fiber layers (GGGG) is smaller than that in pure carbon fiber layers (CCCC), the interfacial damage in the intermediate interfaces in pure glass fiber layers is larger than that in pure carbon fiber layers.

Considering the hybrid configurations without ±45 ° layers (CCGG, GGCC, GCCG, CGGC, GCGC and CGCG), the delamination damage in the first interfaces of all structures having carbon fiber layers on the impact side is smaller than that in the corresponding interfaces of CCCC,

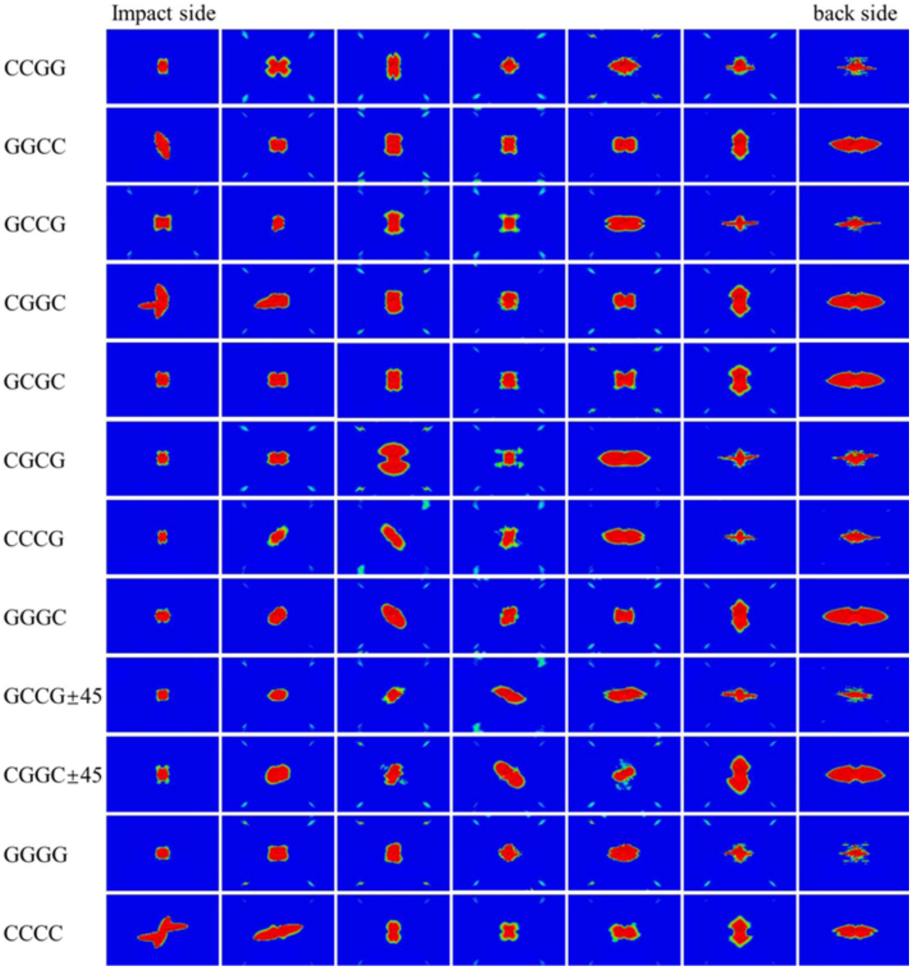

Figure 10. Comparison of delamination damage contours in each interface of hybrid composites under a low-velocity impact of 25 J.

while the delamination damage in the bottom interfaces with carbon fiber layers on the back side is larger. This suggests that while hybridizing with glass layers can help reduce the delamination damage near the impact side, it can result in more serious delamination damage in the carbon layers on the back side.

Considering the hybrid laminates where ±45 ° layers have been introduced, the interface damage between the ±45 ° layers of GCCG±45 is higher as compared to that of the corresponding laminate without ±45 ° layers (GCCG), while delamination damage between the 0 ° and 45 ° layers of configuration GCCG±45 is lower as compared to that in GCCG. The same phenomenon is noted when comparing configurations CGGC and CGGC±45 as well as configurations CCCG and GGGC. Considering all ten of the hybrid laminates, the shape of the interface damage in the penultimate interface of laminates having carbon layers as the bottom two layers is similar to that for CCCC, and the shape of the interface damage in the penultimate interface of the laminates having glass layers as the last two layers is similar as that for GGGG. This suggests that the shape of the delamination damage for the penultimate interface depends on the type of fiber used in the last two layers. In summary, unlike matrix damage, interfacial damage between glass layers is generally less than that interfacial damage between carbon layers. When compared to the delamination damage in the other hybrid composites, the delamination damage exhibited in the GCCG±45 configuration is minimal.

Total Damage Area

The total damage areas by adding the area of matrix tensile damage, matrix compression damage and delamination damage for the different hybrid configurations were evaluated, and a histogram of the results is presented in Figure 11. Since the matrix tensile damage area of the back side of the pure glass laminate (GGGG) is very high, the total damage area for this configuration is the largest. When no ±45 ° layers are present, the damage area for configuration CCGG, where the carbon layers are on the impact side and the glass layers are on the back side, is 23.93 % higher than that for GGCC, which has the opposite arrangement. In the staggered structures (GCGC and CGCG), the damage area in configuration GCGC (in which the carbon fiber layers are located at the back side of the laminate) is smaller. The configuration having glass fiber layers on the surface and carbon fiber layers in the center (GCCG) has a smaller damage area (13.99 % smaller than that for CGGC). By comparing configuration GCCG to GCGC and by comparing configuration CGGC to CGCG, it can be noticed that the layers near the impact side have the greatest influence on the total damage area. By comparing configuration CCGG to GGCC, configuration GCCG to CGGC, and configuration GCGC to CGCG, the total damage area in the hybrid laminates having glass fiber layers on the impact side is smaller than that in laminates having carbon fiber layers on the impact side. Similar to the trend for energy absorption, the damage area for configuration GCCG±45, which has ±45 ° layers added to carbon fiber layers, is 4.73 % smaller than that for the corresponding laminate GCCG without ±45 ° layers , while the incorporation of ±45 ° layers in the glass fiber layers of CGGC±45 has little effect on the size of the damage area when compared to the damage area of the CGGC laminate. Due to the presence of ±45 ° layers, configuration CCCG shows the smallest area of damage and, thus, has the best impact resistance.

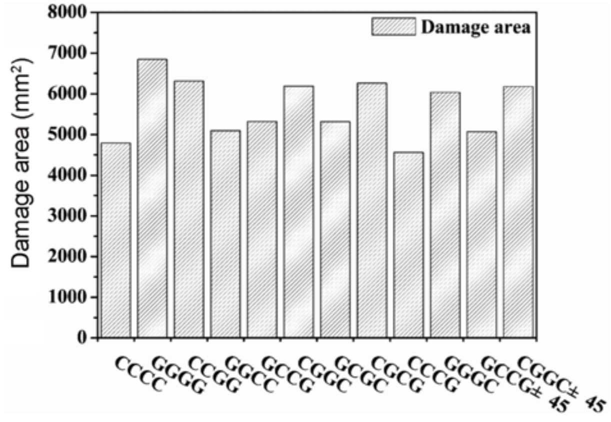

Figure 11. Comparison of total damage area for different configurations.

Conclusion

In this study, the low-velocity impact behavior and impact resistance of hybrid composite laminates reinforced by carbon fibers and glass fibers were numerically simulated and analyzed. The constitutive and progressive damage models for the composite materials and the finite element models for carbon fibers and glass fibers were established and validated. Accordingly, FE models of hybrid composite laminates were established and the impact characteristics—including the global mechanical response, the distribution of damage, and the area of damage in the hybrid configurations—were systematically investigated. Some conclusions of this study are listed as follows:

1. Except for CCCG, the global mechanical response (peak force and maximum displacement) of the hybrid composites is between the responses for the pure carbon fiber laminate and the pure glass fiber laminate, and most hybrid composites are able to absorb more energy than reinforced laminates made from a single type of fiber.
2. Matrix damage in the glass fiber layers is larger than that in the carbon fiber layers, while delamination damage between glass fiber layers on the impact side and the back side of the laminate is smaller than that for carbon fiber layers. Except for configuration CCCG, the total area of damage for hybrid composites is between the areas for

pure carbon fiber laminates and pure glass fiber laminates.

3. The introduction of ±45 ° layers has different effects on carbon fiber layers and glass fiber layers, and their influence on the carbon fiber layers is greater. The addition of ±45 ° layers to carbon fiber layers can enhance the peak force of the laminate and reduce the total area of damage, thereby reducing the absorbed energy and the damping index.
4. The total damage area of the CCCG structure is the smallest because the carbon fiber layers with ±45 ° layers are located on the front side of the laminate, and glass fiber layers are located on the back side of the laminate. The CCCG laminate is configured for the best impact resistance due to the smallest area of damage and the maximum peak force.

Acknowledgement

This work was supported by the National Natural Science Foundation of China (Grant No. 11772267), the 111 Project (Grant No. BP0719007), and the Shaanxi Key Research and Development Program for International Cooperation and Exchanges (Grant No. 2019KW-020).

References

1. X. Lou, H. Cai, P. Yu, F. Jiao, and X. Han, *Compos. Struct.*, **163**, 238 (2017).
2. Q. Meng and Z. Wang, *Polym. Compos.*, **38**, 2536 (2017).
3. Z. Zhao, H. Dang, C. Zhang, G. J. Yun, and Y. Li, *Compos. Part A Appl. Sci. Manuf.*, **110**, 113 (2018).
4. F. Sarasini, J. Tirillò, L. Ferrante, M. Valente, T. Valente, L. Lampani, P. Gaudenzi, S. Cioffi, S. Iannace, and L. Sorrentino, *Compos. Part B Eng.*, **59**, 204 (2014).
5. S. Patel and C. G. Soares, *Compos. Struct.*, **200**, 659 (2018).
6. H. Miao, Z. Wu, Z. Ying, and X. Hu, *Compos. Struct.*, **227**, 111343 (2019).
7. S. Z. H. Shah, S. Karuppanan, P. S. M. Megat-Yusoff, and Z. Sajid, *Compos. Struct.*, **217**, 100 (2019).
8. I. Živković, C. Fragassa, A. Pavlović, and T. Brugo, *Compos. Part B Eng.*, **111**, 148 (2017).
9. M. V. Hosur, M. Adbullah, and S. Jeelani, *Compos. Struct.*, **67**, 253 (2005).
10. M. Tehrani, H. Nosraty, M. Mehrdad, G. Minak, and D. Ghelli, *Mater. Des.*, **31**, 3835 (2010).
11. M. Sayer, N. B. Bektas, and O. Sayman, *Compos. Struct.*, **92**, 1256 (2010).
12. A. K. Barouni and H. N. Dhakal, *Compos. Struct.*, **226**, 111224 (2019).
13. S. N. A. Safri, M. T. H. Sultan, M. Jawaid, and K. Jayakrishna, *Compos. Part B Eng.*, **133**, 112 (2018).
14. P. Hung, K. Lau, L. Cheng, J. Leng, and D. Hui, *Compos. Part B Eng.*, **133**, 86 (2018).
15. I. Papa, L. Boccarusso, A. Langella, and V. Lopresto, *Compos. Struct.*, **232**, 111571 (2020).
16. T. S. Reddy, K. Mogulanna, K. G. Reddy, P. R. S. Reddy, and V. Madhu, *Procedia Struct. Integr.*, **14**, 265 (2019).
17. G. Kretsis, *Compos.,* **18**, 13 (1987).
18. K. S. Pandya, C. Veerraju, and N. K. Naik, *Mater. Des.*, **32**, 4094 (2011).
19. C. Dong and I. J. Davies, *Compos. Part B Eng.*, **72**, 65 (2015).
20. M. Kalantari, C. Dong, and I. J. Davies, *Compos. Struct.*, **138**, 264 (2016).
21. N. K. Naik, R. Ramasimha, H. Arya, S. V. Prabhu, and N. ShamaRao, *Compos. Part B Eng.*, **32**, 565 (2001).
22. Z. Khan, *Adv. Mater. Res.*, **488**, 501 (2012).
23. Y. Swolfs, Y. Geboes, L. Gorbatikh, and S. T. Pinho, *Compos. Part A Appl. Sci. Manuf.*, **103**, 1 (2017).
24. D. Chen, Q. Luo, M. Meng, and G. Sun, *Compos. Part B Eng.*, **176**, 107191 (2019).
25. Y. Hu, W. Liu, and Y. Shi, *Compos. Struct.*, **216**, 127 (2019).
26. A. K. Bandaru, S. Patel, S. Ahmad, and N. Bhatnagar, *J. Compos. Mater.*, **52**, 877 (2018).
27. N. Hongkarnjanakul, C. Bouvet, and S. Rivallant, *Compos. Struct.*, **106**, 549 (2013).
28. H. Singh, K. K. Namala, and P. Mahajan, *Compos. Part B Eng.*, **76**, 235 (2015).
29. J. P. Hou, N. Petrinic, and C. Ruiz, *Compos. Sci. Technol.*, **61**, 2069 (2001).
30. J. P. Hou, N. Petrinic, and C. Ruiz, *Compos. Sci. Technol.*, **60**, 273 (2000).
31. W. Tan, B. G. Falzon, L. N. S. Chiu, and M. Price, *Compos. Part A Appl. Sci. Manuf.*, **71**, 212 (2015).
32. X. Li, D. Ma, H. Liu, W. Tan, X. Gong, C. Zhang, and Y. Li, *Compos. Struct.*, **207**, 727 (2019).
33. C. S. Lee, J. H. Kim, S. K. Kim, D. M. Ryu, and J. M. Lee, *Compos. Struct.*, **121**, 406 (2015).
34. P. F. Liu, B. B. Liao, L. Y. Jia, and X. Q. Peng, *Compos. Struct.*, **149**, 408 (2016).
35. V. S. Sokolinsky, K. C. Indermuehle, and J. A. Hurtado, *Compos. Part A Appl. Sci. Manuf.*, **42**, 1119 (2011).
36. M. L. Benzeggagh and M. Kenane, *Compos. Sci. Technol.*, **56**, 439 (1996).
37. T. S. Reddy and K. Mogulanna, *Procedia Struct. Integr.*, **14**, 265 (2019).
38. I. Lapczyk and J. A. Hurtado, *Compos. Part A Appl. Sci. Manuf.*, **38**, 2333 (2007).
39. P. Zhang, Y. Feng, T. Q. Bui, X. Hu, and W. Yao, *Compos. Struct.*, **232**, 111551 (2020).
40. J. Zhi and T. E. Tay, *Comput. Meth. Appl. Mech. Eng.*, **351**, 60 (2019).
41. S. Chen, M. Zang, and W. Xu, *Comput. Meth. Appl. Mech. Eng.*, **294**, 72 (2015).
42. G. Vigueras, F. Sket, C. Samaniego, L. Wu, L. Noels, D. Tjahjanto, E. Casoni, G. Houzeaux, A. Makradi, J. M. Molina-Aldareguia, M. Vázquez, and A. Jérusalem, *Compos. Struct.*, **125**, 542 (2015).

43. S. Chen, N. Mitsume, W. Gao, T. Yamada, M. Zang, and S. Yoshimura, *Comput. Struct.*, **215**, 80 (2019).
44. S. Chen, N. Mitsume, and T. Q. Bui, *Compos. Struct.*, **229**, 111406 (2019).
45. B. B. Liao and P. F. Liu, *Compos. Struct.*, **159**, 567 (2017).
46. R. Ren, J. Zhong, G. Le, and D. Ma, *Compos. Struct.*, **220**, 481 (2019).
47. Z. Wang and J. Zhao, *Thin-Walled Struct.*, **144**, 106321 (2019).